

Article

Joining 3YSZ Electrolyte to AISI 441 Interconnect Using the Ag Particle Interlayer: Enhanced Mechanical and Aging Properties

Xiaoqing Si *, Xiaoyang Wang, Chun Li, Tong Lin , Junlei Qi and Jian Cao

State Key Laboratory of Advanced Welding and Joining, Harbin Institute of Technology, Harbin 150001, China; 21B309037@stu.hit.edu.cn (X.W.); chun.li@hit.edu.cn (C.L.); 19B909118@stu.hit.edu.cn (T.L.); jlqi@hit.edu.cn (J.Q.); cao_jian@hit.edu.cn (J.C.)

* Correspondence: sixq@hit.edu.cn

Abstract: Reactive air brazing has been widely used in fabricating solid oxide fuel/electrolysis cell (SOFC/SOEC) stacks. However, the conventional Ag–CuO braze can lead to (I) over oxidation at the steel interconnect interface caused by its adverse reactions with the CuO and (II) many voids caused by the hydrogen-induced decomposition of CuO. The present work demonstrates that the Ag particle interlayer can be used to join yttria-stabilized zirconia (YSZ) electrolytes to AISI 441 interconnect in air instead of Ag–CuO braze. Reliable joining between YSZ and AISI 441 can be realized at 920 °C. A dense and thin oxide layer (~2 μm) is formed at the AISI 441 interface. Additionally, an interatomic joining at the YSZ/Ag interface was observed by TEM. Obtained joints displayed a shear strength of ~86.1 MPa, 161% higher than that of the joints brazed by Ag–CuO braze (~33 MPa). After aging in reducing and oxidizing atmospheres (800 °C/300 h), joints remained tight and dense, indicating a better aging performance. This technique eliminates the CuO-induced issues, which may extend lifetimes for SOFC/SOEC stacks and other ceramic/metal joining applications.



Citation: Si, X.; Wang, X.; Li, C.; Lin, T.; Qi, J.; Cao, J. Joining 3YSZ Electrolyte to AISI 441 Interconnect Using the Ag Particle Interlayer: Enhanced Mechanical and Aging Properties. *Crystals* **2021**, *11*, 1573. <https://doi.org/10.3390/cryst11121573>

Academic Editor: Vladislav V. Kharton

Received: 15 November 2021
Accepted: 13 December 2021
Published: 16 December 2021

Publisher's Note: MDPI stays neutral with regard to jurisdictional claims in published maps and institutional affiliations.



Copyright: © 2021 by the authors. Licensee MDPI, Basel, Switzerland. This article is an open access article distributed under the terms and conditions of the Creative Commons Attribution (CC BY) license (<https://creativecommons.org/licenses/by/4.0/>).

Keywords: solid oxide fuel/electrolysis cells; sintering; YSZ; Ag particle interlayer; aging

1. Introduction

As electrochemical energy conversion devices, solid oxide fuel/electrolysis cells (SOFCs/SOECs) are increasingly widely applied in practice due to high efficiency, fuel diversity, and ultra-low pollution [1–5]. YSZ ceramics, possessing excellent fracture toughness, chemical stability, and high ionic conductivity at elevated temperatures, have become the most successful and commonly used electrolyte for SOFCs/SOECs [6–10]. Typically, single cells are combined into SOFC/SOEC stacks to obtain sufficiently high voltage [11,12]. To date, the planar SOFC/SOEC design achieves the broadest applications due to its easy stacking characteristics [13–15]. The most critical process in fabricating the planar stack is the sealing between solid oxide cells and ferritic stainless steel interconnects [16]. Ferritic stainless steel usually possesses excellent mid-temperature stability performance because of the dense Cr₂O₃ layer on the substrate surface caused by the high Cr content [17–19]. The joining between solid oxide cells and ferritic stainless steel should be stable during the subsequent long-term high-temperature service [20,21].

Glass/glass-ceramic bonding and reactive air brazing (RAB) are currently two promising methods to join cells to interconnects [22–24]. For the glass/glass-ceramic materials, their composition can be tailored to match the thermomechanical requirements of the SOFC/SOEC stack components [25–27]. However, problems such as the crystallization during sintering/operation and inherent brittleness of the glass-based sealants may be detrimental to the long-term stability of joints [28,29]. Fortunately, RAB is an alternative technique to satisfy the sealing requirements without the above issues. This method can be performed directly in air with a noble metal (Ag, Pt, Au, Pd)-oxide (CuO, V₂O₅, Nb₂O₅, SiO₂) braze system [30–32]. The oxide modifies or reacts with the substrate surface, thus promoting the wetting behavior of the braze on the newly formed surface [33]. Up to now,

the Ag–CuO is the most effective and commonly used RAB braze for joining SOFC/SOEC components [34–36].

However, recent studies have pointed out that the introduction of CuO can give rise to two significant issues. One is the thick and loose Cu/Cr/Mn/Fe-oxide layer (typically $\geq 20 \mu\text{m}$) at the braze/interconnect interface due to the reaction between the CuO from the braze and the steel interconnect [31,37,38]. Moreover, the rapid growth of this oxide layer has been proven to be a key factor for the RAB joint failure during aging [22]. Another issue for the Ag–CuO braze is that CuO is thermodynamically unstable when exposed to the reducing atmosphere in fuel (i.e., anode) chambers [7,36]. The decomposition of CuO through the reaction $\text{CuO} + \text{H}_2 \rightarrow \text{Cu} + \text{H}_2\text{O}$ and the subsequent solid solution of Cu into the Ag matrix can lead to many voids [3,39]. Besides, these voids can offer rapid paths for hydrogen permeation into the joint central region (where the hydrogen reacts with diffused oxygen to generate gaseous water pockets), consequently weakening the gas-tightness and mechanical properties of joints [36,40–42].

However, it has been noted that the joints mainly composed of Ag with good plasticity still have an irreplaceable role when the SOFC/SOEC stack is used as a mobile device [43,44]. Hence, a sealant without CuO should be tested to solve the problems caused by the CuO-containing braze, and a pure Ag interlayer might be a good choice. Molten Ag may not provide a sufficient joining for the YSZ-electrolyte/steel-interconnect structure in the SOFC/SOEC stack considering the limited wettability of liquid Ag on the YSZ electrolyte. However, nano- or micron-sized Ag particles have specific sintering properties, which can form effective joining below the melting point of Ag ($961.8 \text{ }^\circ\text{C}$) [45,46]. Therefore, this work intends to apply the Ag particle interlayer to replace the Ag–CuO braze for joining the YSZ electrolyte and AISI 441 interconnect below the melting point of Ag. The benefits of this approach are apparent: (I) The oxide layer at the interconnect interface can be effectively mitigated due to the absence of CuO; (II) The decomposition of CuO and the consequent damage to the joint stability are entirely avoided; (III) The joining temperature is lowered compared with the typical RAB process, thus weakening the interconnect oxidation; and (IV) The overflow of braze in traditional braze methods (such as vacuum brazing, glass/glass-ceramic bonding, RAB, etc.) can be solved. However, whether a high-strength joining between the YSZ-electrolyte and steel-interconnect can be achieved without the CuO modification is unclear. Furthermore, the aging performance of joints should also be studied in detail.

In this study, a pure Ag particle interlayer was used to join the YSZ electrolyte to the AISI 441 interconnect directly in air. The microstructure, formation mechanism, mechanical properties, and the effects of joining temperature on the joint were studied in-depth. Furthermore, the long-term stability of joints both in oxidizing and reducing atmospheres was also evaluated.

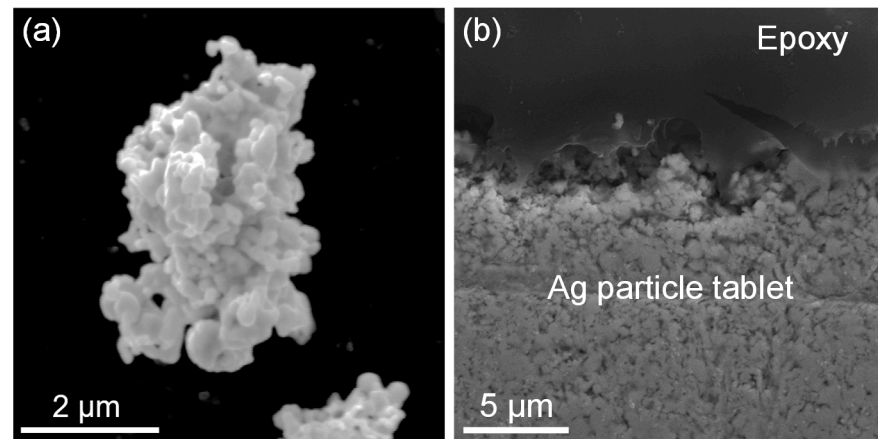
2. Experimental Procedures

2.1. Materials

The YSZ electrolyte (containing 3 mol% yttria) adopted in this work was purchased from Shanghai Unite Technology Co. Ltd. (Shanghai, China). The reason we chose 3YSZ is that it possesses excellent mechanical properties and moderate ionic conductivity. AISI 441 stainless steel (a kind of ferritic stainless steel) to be joined was obtained from Baowu Iron and Steel Group Co. Ltd., Shanghai, China, with a thickness of $\sim 2 \text{ mm}$, and its chemical composition is displayed in Table 1. The chemical composition was characterized by a spark emission spectrometer (Germany) using the ASTM E1086-14 standard. Ag powder (Aladdin, Shanghai, China 99.95%, $\leq 10 \mu\text{m}$) was pressed (200 MPa, 180 s) into a $\sim 100 \mu\text{m}$ -thick tablet via a tableting instrument. The morphology of the Ag powder and Ag tablet is shown in Figure 1a,b.

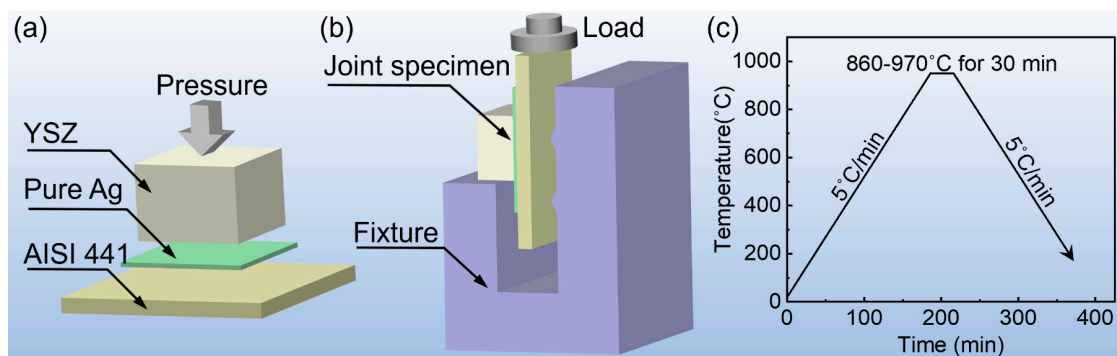
Table 1. Composition of the AISI 441 stainless steel (wt.%).

	Cr	Mn	Si	Nb	Ti	Al	Fe
Content	17.53	0.40	0.59	0.41	0.17	0.07	Balance

**Figure 1.** (a) Morphology of the Ag powder and (b) morphology of the Ag particle tablets.

2.2. Joining Process

Before joining, AISI 441 stainless steel was cut into $10 \times 10 \times 2 \text{ mm}^3$ pieces using a wire electric discharge machine and subsequently polished with 1200- abrasive paper. YSZ ceramics were cut into $5 \times 5 \times 3 \text{ mm}^3$ specimens using a diamond wire saw, then both the AISI 441 pieces and YSZ specimens were ultrasonically cleaned in ethanol for 20 min. The Ag tablet was sandwiched between the YSZ and AISI 441. Meanwhile, pressure ($\sim 2 \text{ MPa}$) is applied on the top of the sandwich to ensure tight contact during joining, as shown in Figure 2a. Finally, these assemblies were sintered in a muffle furnace (KSL-1400X) and heated at a series of temperatures ($860\text{--}970 \text{ }^\circ\text{C}$) for 30 min, with heating and cooling rates of $5 \text{ }^\circ\text{C}/\text{min}$ (see temperature curve in Figure 2c). The whole joining process was carried out in quasi-static air.

**Figure 2.** (a) Schematic diagram of joining assembly. (b) Sketch of the shear test. (c) Joining temperature curve.

2.3. Long-Term Tests in Reducing and Oxidizing Atmospheres

Two groups of tests were conducted to assess the long-term stability of the joints in reducing and oxidizing atmospheres. In both tests, the obtained joints were placed in an alumina crucible, exposed in a horizontal tube furnace (OTF-1200X), and heated at $800 \text{ }^\circ\text{C}$ for 300 h (heating and cooling rates of $5 \text{ }^\circ\text{C}/\text{min}$). To simulate the reducing atmosphere in the fuel chamber, the compressed gas ($5\% \text{ H}_2 + 95\% \text{ Ar}$) flowed through a water container (heated to $80 \text{ }^\circ\text{C}$ for 50% humidity) to obtain a wet reducing atmosphere containing 50% ($\text{H}_2 + \text{Ar}$) and 50% H_2O , as shown in Figure S1. Meanwhile, the gas flow was kept at 6 L/h .

As for the aging test in the oxidizing atmosphere, the compressed air flowed into the above horizontal tube furnace with a constant gas flow of 6 L/h.

2.4. Microstructural Characterization and Shear Test

To observe the microstructure of the YSZ/AISI 441 joints, cross-section samples of joints at each parameter were obtained by the diamond wire cutting method. Then, these samples were embedded in epoxy resin. The cross-sections were ground, in turn, with 400, 600, 800, 1000, and 2000-grit silicon carbide papers and subsequently polished with colloidal silica suspension (OPS). Finally, scanning electron microscopy (SEM, Quanta 200FEG, USA) combined with an energy dispersive spectrometer (EDS) was adopted for metallographic observation.

For further analysis at the YSZ/Ag interface, a focused ion beam (FIB, Helios Nano Lab 600i, USA) was used to prepare the sample with a thickness of 50–100 nm. Subsequently, this sample was analyzed by a transmission electron microscope (TEM, Talos F200X, USA).

A universal mechanical testing machine (Instron 1186, Norfolk County, MA, USA) was used to measure the shear strength of the joint. The schematic illustration of the shear test was depicted in Figure 2b. Five samples were measured, and numerical results were averaged at each temperature.

3. Results and Discussion

3.1. Interfacial Microstructure and Formation Mechanism of YSZ/AISI 441 Joint

Figure 3a displays the overall SEM image of the YSZ/AISI 441 joint obtained with the Ag particle interlayer at 920 °C/30 min in air. It is apparent that a tight joint was formed under this condition, and the Ag particle interlayer was completely densified without any voids after sintering. This completely dense interlayer structure can block the gas in the anode chamber and cathode chamber. Furthermore, compared with the RAB process, this technology eliminates the pores caused by CuO reduction during operation, which can significantly prolong the service life of joints. Both the YSZ/Ag interface and the AISI 441/Ag interface seem compact and defect-free. The corresponding enlarged SEM images (Figure 3(a₁,a₂)) were obtained for further details about these two interfaces.

A thin and dense oxide layer (~2 μm) formed between Ag and AISI 441 (Figure 3(a₂)), which has been proven to be composed of (Fe, Mn, Cr)₃O₄ and Cr₂O₃ in many studies [31,47–49]. It is worth noting that the oxide layer formed at the stainless steel interface by the traditional RAB method is typically thicker than 20 μm [31,37,38], which is 10 times wider than the above oxide layer. This thick and loose oxide layer can cause crack initiation and poor gas tightness, and its further growth during service results in joint failure. The dramatic reduction in the oxidation layer thickness is due to the absence of CuO and the lower joining temperature (920 °C, while the traditional RAB method generally requires temperatures higher than 970 °C). Compared with the ≥20 μm thick oxide layer, this thin and dense oxidation layer may help maintain the long-term stability of the joint. Moreover, the oxide layer on the AISI 441 surface increases the total resistance of the interconnect, thereby increasing the ohmic resistance of the stack [50,51]. Therefore, compared with RAB, the thinner oxide layer obtained by the Ag particle interlayer can bring lower area specific resistance (ASR), which helps maintain the high efficiency of stacks.

It can be seen from the enlarged view in Figure 3(a₁) that the YSZ/Ag interface is dense without micro-voids or micro-cracks. It is well documented that a tight atomic bonding is essential to fabricate a stable joint [52], while it is hard to judge whether there is atomic bonding between YSZ and Ag only by SEM. Therefore TEM was adopted to further analyze the YSZ/Ag interface. Figure 3b exhibits the bright-field image at the YSZ/Ag interface, and the corresponding elemental distribution (Zr and Ag) is shown in Figure 3c. The element distribution indicates that Ag and YSZ are closely joined without apparent gaps. The enlarged view in Figure 3(c₁) reveals that a small number of Ag atoms diffuse into the YSZ, forming a diffusion layer with a width of ~3 nm. As shown in Figure 3d, the elemental distributions of Ag, Zr, and O along the yellow line in Figure 3b also indicate

that a diffusion layer (~ 3 nm) exists between Ag and YSZ. This diffusion phenomenon might play a crucial role in forming a hermetic joint. High resolution transmission electron microscope (HRTEM) was used to determine the bonding type between YSZ and Ag. The HRTEM image in Figure 3e shows that the crystal lattices of Ag and YSZ are clearly visible. The enlarged view (Figure 3(e₁)) of region 4 and the corresponding selected area diffraction patterns (SAPDs) (Figure 3(e₂,e₃)) note that the [220] zone axis of the ZrO₂ is parallel to the [011] axis of the Ag. In addition, a disordered lattice region (~ 3 nm) was observed between Ag and YSZ, which could be attributed to the diffusion of Ag into the YSZ. The above TEM analysis demonstrates that atomic bonding was achieved between YSZ and Ag, which is the premise of obtaining an airtight joint with superior mechanical properties.

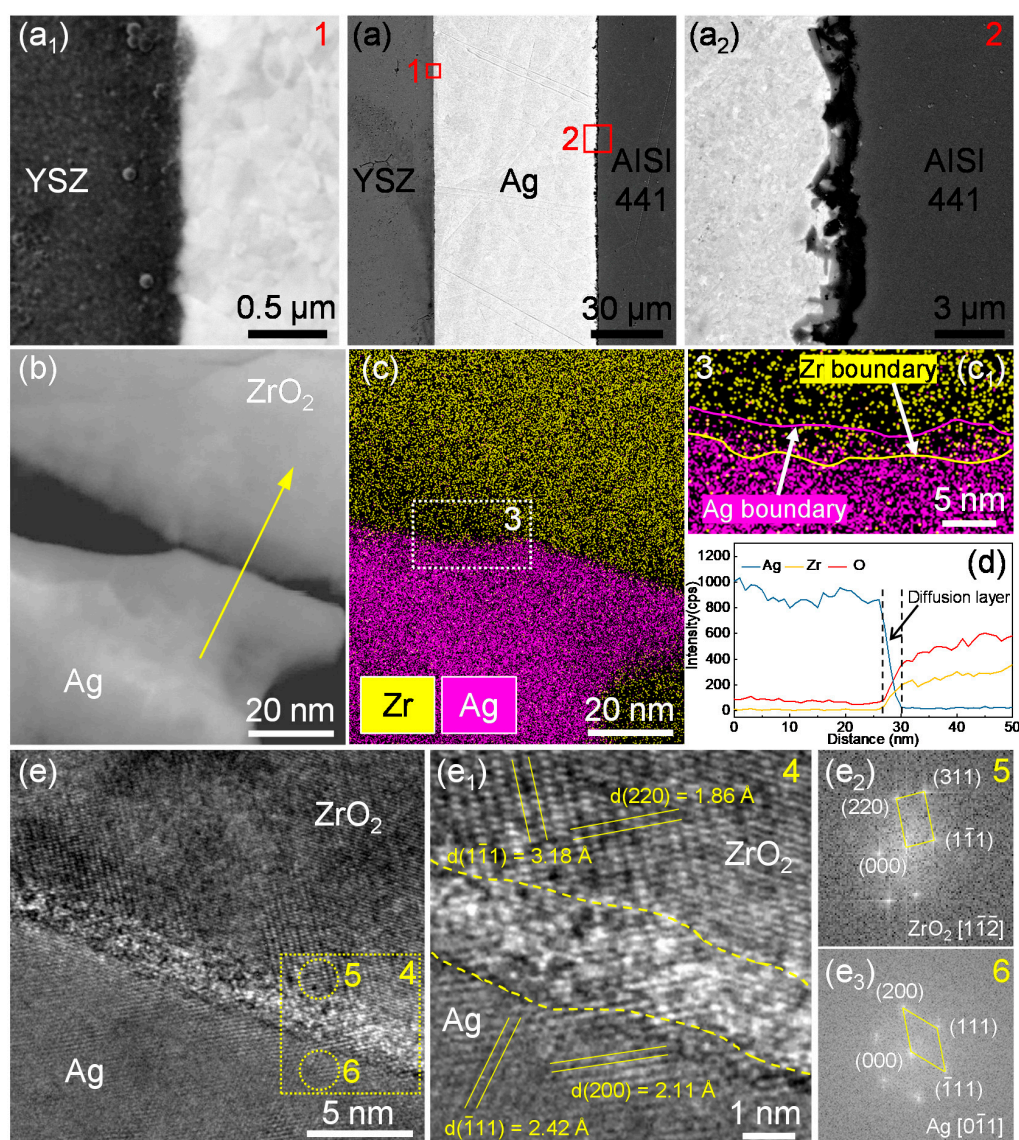


Figure 3. (a) Microstructure of YSZ/AISI 441 joint obtained at 920 °C, enlarged view at (a₁) YSZ and (a₂) AISI 441 interface; (b) bright-field image at the YSZ/Ag interface, (c) corresponding EDS mapping results, (c₁) enlarged view of region 3, (d) elemental distributions along the yellow line, (e) HRTEM image at YSZ/Ag interface, (e₁) enlarged view of region 4, selected area diffraction patterns of (e₂) region 5 and (e₃) 6.

It can be seen from Figure 1b that micron-level or even nano-level Ag particles still existed in the Ag tablets after dry pressing. Therefore, the sintering effect might be one reason for the successful joining of YSZ and AISI 441. The driving force of sintering

primarily depends on the inherently high surface energy and curved surface of the Ag particles [53]. Furthermore, the Laplace equation can well describe the driving force for interfacial sintering, as shown in the following equation [54].

$$P = P_0 + \gamma \left(\frac{1}{R_1} + \frac{1}{R_2} \right)$$

where P is the driving force for interfacial sintering and P_0 represents the external pressure; γ is the surface energy, determined by surface stress derivation and surface chemical contribution of the particles; and R_1 and R_2 are the particles' curvature radii at the contact point. Given the even surface of the YSZ, it can be considered that the YSZ in contact with the Ag particle has a huge curvature radius (i.e., $R_2 \rightarrow \infty$). Accordingly, the driving force mainly depends on the curvature radius of the Ag particle (R_1), as shown in Figure 4a. Moreover, the pressure of ~2 MPa applied during the joining process can result in a large external pressure P_0 , thereby further increasing the interfacial sintering driving force P . Consequently, the sintering driving force at the Ag/YSZ interface is large enough to form effective Ag/YSZ bonding. The joining mechanism at the AISI 441 interface is similar to that described above. During joining, a dense oxide layer is generated on the AISI 441 surface. Ag particles form an effective joining with the oxide layer on the AISI 441 surface under a similar sintering driving force.

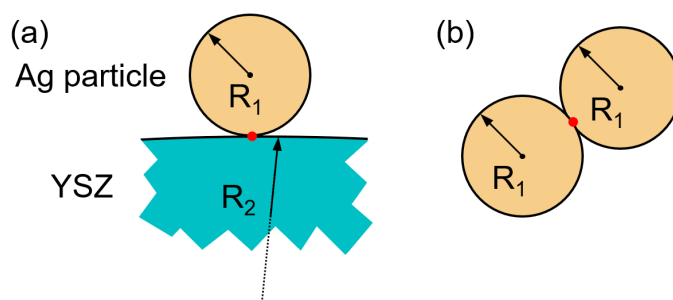


Figure 4. (a) Schematic diagram of Ag particle sintering with YSZ. (b) Schematic diagram of Ag particle sintering with adjacent Ag particle.

The schematic diagram of the joining among Ag particles is shown in Figure 4b. According to the Laplace equation, the sintering driving force here is greater than that at the interface. Therefore, adequate bonding is formed among the Ag particles under this sintering driving force.

The formation mechanism of the above joint is similar to the joint obtained by commercial Ag nano paste sintering joining to some extent. However, the joint obtained by traditional Ag nano paste (sintered at 280–400 °C) possesses a high pore fraction and low mechanical properties, which cannot be used to seal SOFCs/SOECs [55,56]. In contrast, a fully dense joint with good mechanical properties (see Section 3.3) can be obtained using the silver particle interlayer, which can well meet the long-term operation requirements of SOFCs/SOECs. In addition, the complex preparation process and high cost of Ag nano paste are key factors limiting its wider application [46,57]. Conversely, the preparation of a Ag particle interlayer is low-cost (~1/10 of that of Ag nano paste) and straightforward, which may promote the rapid commercialization of this technology.

3.2. Effect of Joining Temperature on YSZ/AISI 441 Joint

Since the joining temperature is an essential factor affecting the microstructure and properties of the joint, the microstructures of the joints obtained at various joining temperatures (860–970 °C) for 30 min can be observed in this section, as displayed in Figure 5.

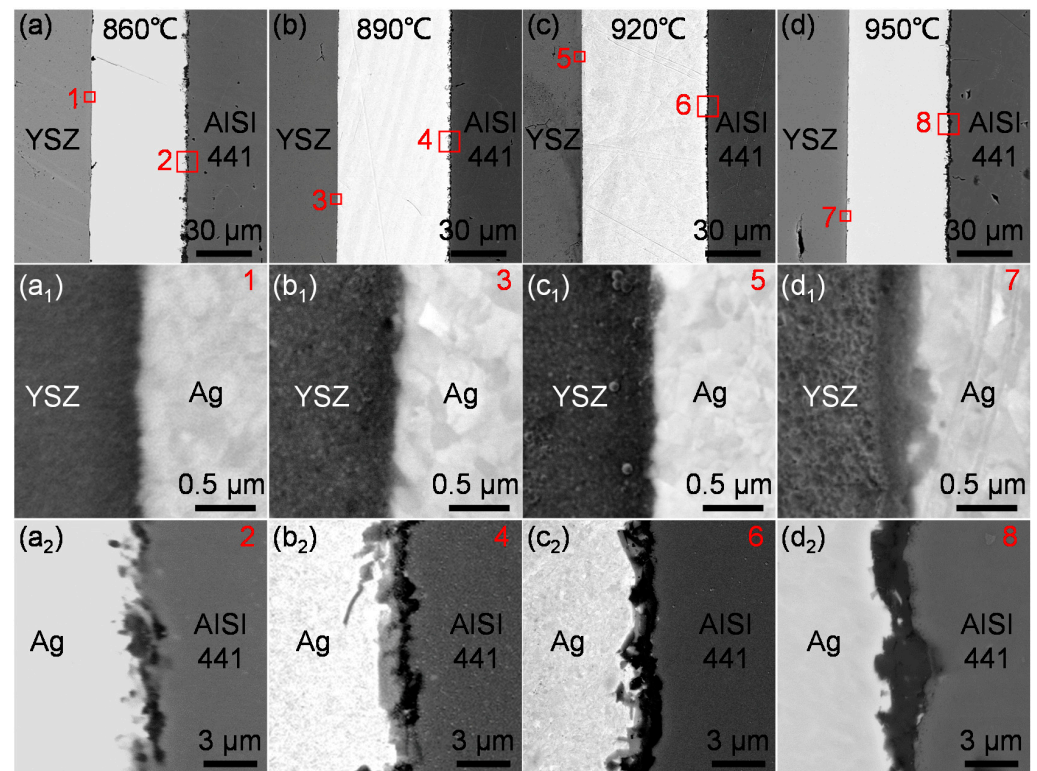


Figure 5. Microstructure of joints obtained at (a) 860 °C, (b) 890 °C, (c) 920 °C, and (d) 950 °C; (a₁–d₁) enlarged view at the YSZ/Ag interface; (a₂–d₂) enlarged view at the Ag/AISI 441 interface.

It can be seen from Figure 5a–d that well-formed joints could be obtained at 860–950 °C. The enlarged view at the YSZ/Ag interface (Figure 5(a₁–d₁)) exhibited no defects or voids observed at this interface at 860–950 °C. This can mainly be attributed to the sintering effect of Ag particles (explained in Section 3.1). Furthermore, Ag is soft enough to fill the gaps at this interface under the pressure of ~2 MPa, which is another contributor. Furthermore, since there is no reaction product between Ag and YSZ, and both are stable at 860–950 °C, no noticeable change of the YSZ/Ag interfacial microstructure at various temperatures can be observed by SEM.

For the AISI 441/Ag interface (see Figure 5(a₂–d₂)), the oxidation behavior is intensified with elevating temperatures. At 860 °C (Figure 5(a₂)), a discontinuous oxide is formed at the AISI 441 interface. The oxide layer is thickened with the increasing temperature, and a continuous and dense oxide layer (2–3 µm in thickness) was observed at 950 °C (Figure 5(d₂)). In addition, when the temperature reached 970 °C (higher than the melting point of Ag), the joint quality decreased significantly, as seen in the Supplementary Materials (Figure S2). Most Ag flowed away from the gap between YSZ and AISI 441, and only a slight residual Ag existed between YSZ and AISI 441. This phenomenon can be attributed to the high contact angle of pure Ag on the YSZ surface and no reaction between YSZ and Ag, resulting in the loss of liquid Ag during sintering [39,58].

3.3. Shear Strength of Joints at Various Joining Temperatures

Shear strength is an essential indicator for measuring the joint quality, so shear tests were conducted for the joints obtained at different temperatures. Results are reported in this section. Subsequently, the fracture surfaces after the shear tests were analyzed by SEM to further understand the failure mechanism.

Figure 6a notes that the shear strength of the joint first increased and then decreased with the increasing temperature (from 860 °C to 970 °C), reaching the maximum (~86.1 MPa) at 920 °C. Figure 6b illustrates the AISI 441-side fracture morphology of the joints obtained at 860 °C. The fracture mainly occurs between YSZ and Ag, and no notice-

able dimple on the Ag surface was observed. This phenomenon indicates a poor bonding strength between Ag and YSZ at 860 °C due to insufficient sintering or diffusion between Ag and YSZ at lower temperatures. Hence, the joints exhibited low shear strength at low temperatures (~20.1 MPa at 860 °C). When the joining temperature increased to 890 °C, the shear strength was significantly increased to 64.6 MPa. The fracture morphology in Figure 6c (AISI 441 side) and Figure S3 (YSZ side) showed that part of the fracture began to occur between Ag and AISI 441. On one hand, this was due to the increase in the YSZ/Ag interfacial strength as the temperature rises. On the other hand, the thickening of the oxide layer on the AISI 441 surface may reduce the bonding strength at the AISI 441/Ag interface. The maximum shear strength was reached at 920 °C. The fracture occurred at both the YSZ/Ag interface and the AISI 441/Ag interface (see Figure 6d). Furthermore, many dimples were observed at the Ag layer, indicating a large plastic deformation and high strength at the YSZ/Ag interface [59]. A further increase in temperature will reduce the joint strength (~55.8 MPa at 950 °C), mainly due to the increased oxidation of the AISI 441 surface, as shown in the enlarged view of area 8. It can be seen from Figure 6e and Figure S3 that the fracture mainly occurred at the Ag/AISI 441 interface. Similar conclusions can be obtained from the shear stress–shear displacement curve in Figure S4. A yield platform was observed on the curve of the joint obtained at 920 °C, implying large plastic deformation, corresponding to the dimples in Figure 6d. For the curve of the joint obtained at 950 °C, no obvious platform was found. This is because the oxidation of the 441 surface was intensified at 950 °C, and the fracture mainly occurred near the oxide with poor plasticity. In addition, when the joining temperature rose to 970 °C (exceeding the melting point of Ag), the shear strength dropped sharply to ~2.5 MPa, and the reason for this is explained in detail in Section 3.2.

According to the research of Cao et al. [31], the shear strength of the YSZ/AISI 441 joint obtained using traditional Ag–CuO braze at 960 °C/30 min is ~33 MPa. Surprisingly, the joint strength in this study could reach ~86.1 MPa, which was 161% higher than that of traditional RAB joints. The significant enhancement in shear strength could be explained by the reduced oxidation at the AISI 441 surface at lower joining temperature (920 °C). Meanwhile, the absence of CuO further alleviates the oxidation of the metal surface.

3.4. Stability of Joints in Reducing and Oxidizing Atmospheres

To assess the long-term stability of the joints in SOFC/SOEC relevant atmospheres, the YSZ/441 joints obtained with pure Ag interlayer at 920 °C/30 min were aged for 300 h at 800 °C in 50% (H₂ + Ar) – 50% H₂O and air atmospheres, respectively. The aging results were analyzed as follows.

Figure 7 presents the cross-sectional SEM images of the joints after exposure in 50% (H₂ + Ar) – 50% H₂O at 800 °C for 300 h. Obviously, aging for 300 h in the reducing atmosphere did not cause any significant change in the overall morphology of the joint. No defects (such as delamination, cracks, or voids) due to reduction were observed. The enlarged views of the two interfaces were subsequently observed for further details. It can be seen from Figure 7(a₁–c₁) that the YSZ/Ag interface remained compact and well bonded, and the reducing atmosphere had no apparent effect on this interface. The good reduction resistance of the interface may be attributed to the Ag–ZrO₂ atomic bonding. The AISI 441/Ag interface also showed excellent stability in a reducing atmosphere at 800 °C, as shown in Figure 7(a₂–c₂). The oxide layer at the AISI 441 interface remained compact, and its thickness did not seem to change after exposure to a reducing atmosphere for 300 h. This may be because the oxide layer is thermodynamically stable under this condition and is difficult to decompose by reduction. Notably, the voids caused by the CuO reduction, which is inevitable in the traditional RAB method [3,36,39,42], were completely eliminated.

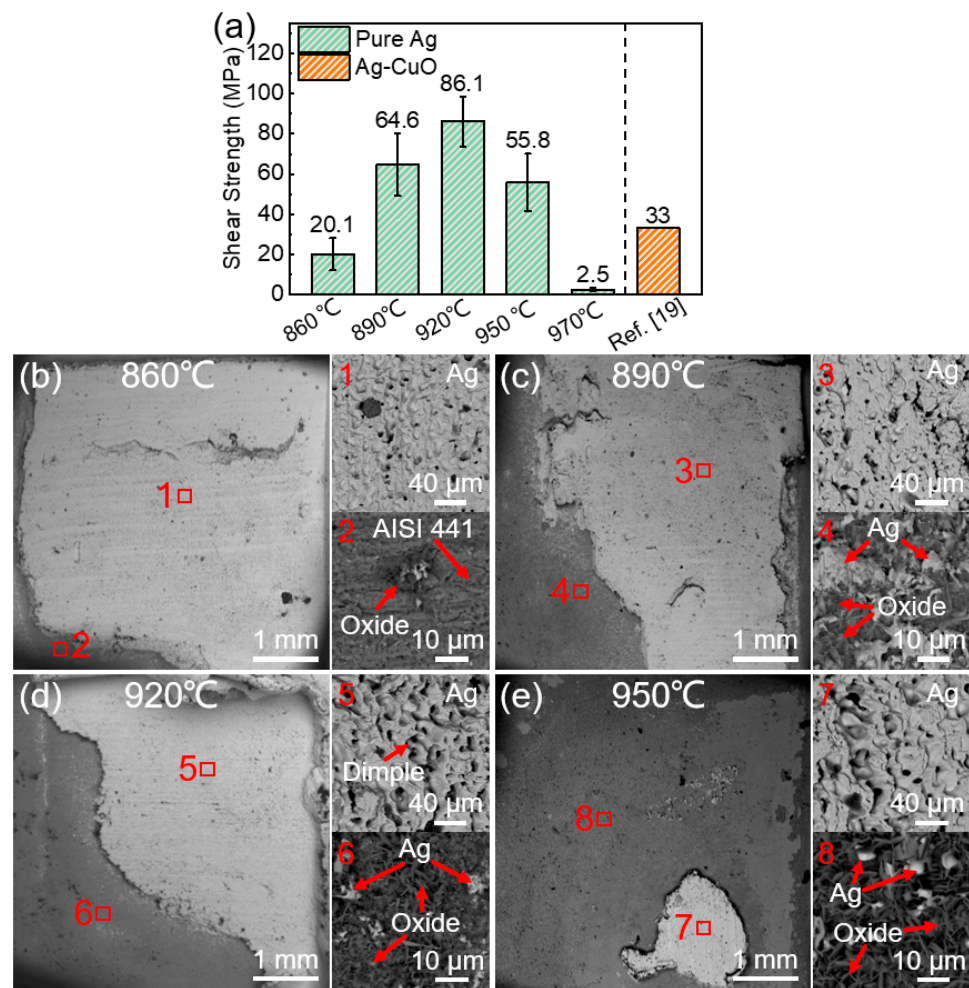


Figure 6. (a) Room-temperature shear strength of the joints obtained at various conditions using the Ag interlayer and Ag–CuO braze; corresponding fracture surfaces at various joining temperatures at the AISI 441 side: (b) 860 °C, (c) 890 °C, (d) 920 °C, and (e) 950 °C.

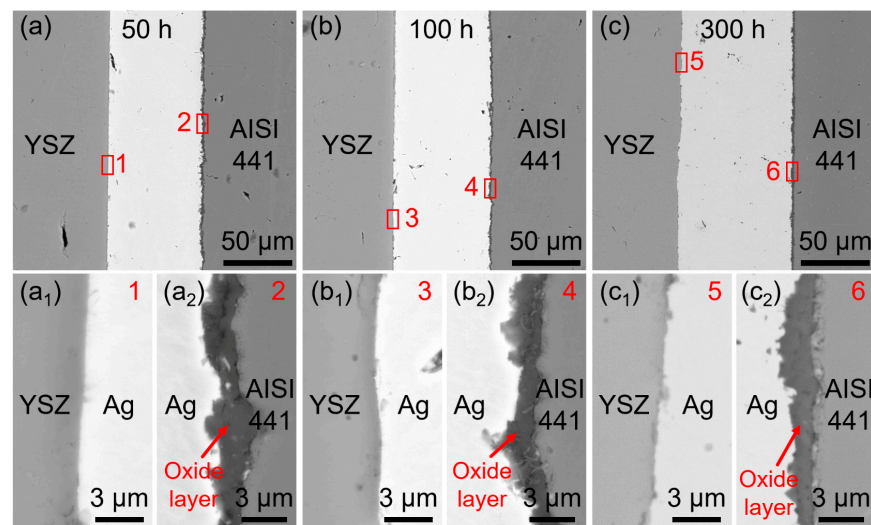


Figure 7. Microstructure of the joints after aging in 50% (H₂ + Ar) – 50% H₂O at 800 °C for (a) 50 h, (b) 100 h, and (c) 300 h, respectively. (a₁–c₁) are enlarged views of the YSZ interface, (a₂–c₂) are enlarged views of the AISI 441 interface).

Figure 8 displays the joint structure after aging in air at 800 °C for 300 h. It can be seen from the low-magnification SEM images in Figure 8a–c that the joints maintained tight bonding in a wide range without delamination after oxidation for 300 h. Furthermore, the oxide layer on the AISI 441 surface was thickened with the increasing oxidation time. Additionally, no apparent defects were observed in cross-sectional SEM images from Figure 8(a₁–c₁). The YSZ/Ag interface remained tight and defect-free (the enlarged view at this interface is not shown). The enlarged view at the AISI 441 interface (Figure 8(a₂–c₂)) showed that the oxide layer thickness only reached ~15 μm after oxidation for 300 h, which was even thinner than that of the joints obtained by the traditional Ag–CuO braze without oxidation test (typically ≥20 μm) [31,37,38]. Furthermore, the oxide layer in this study was denser, and only a few micro-voids appeared after oxidation for 300 h. Both the thickness and compactness of the oxide layer indicated superior oxidation resistance and aging performance of the joints fabricated by the Ag particle interlayer. Meanwhile, the stack obtained through the Ag particle interlayer should have smaller ohmic resistance and higher efficiency in the operation atmosphere, especially in a high-temperature oxidizing atmosphere. It must be noted that there were some differences between the test conditions in this research (separate aging tests in oxidation and reduction atmosphere, respectively) and the actual operating conditions (dual atmosphere) in stacks, so the above results are only limited reference.

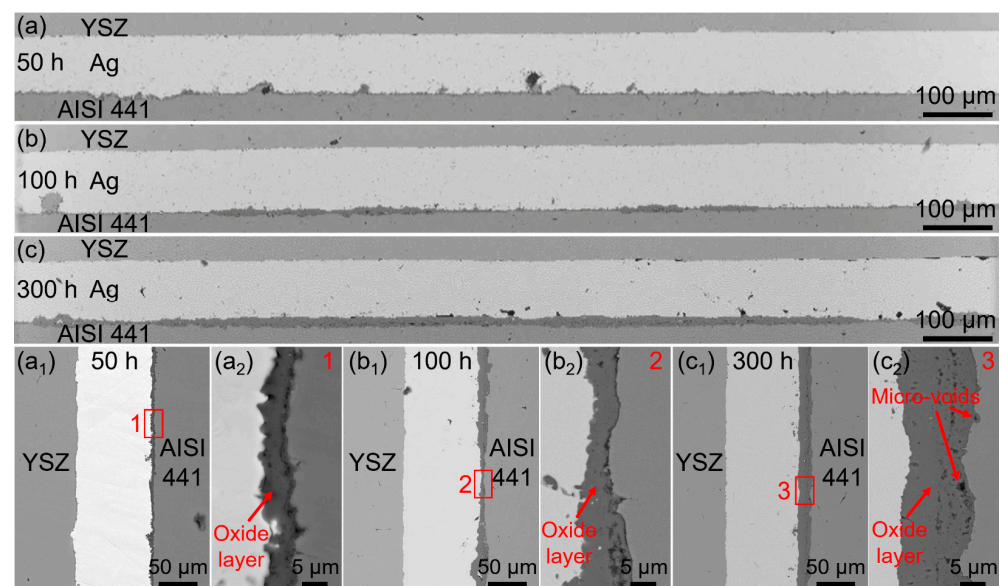


Figure 8. Overview of the SEM image of the joints after aging in air at 800 °C for (a) 50 h, (b) 100 h, and (c) 300 h, respectively. (a₁–c₁) are interfacial microstructure of joints, (a₂–c₂) are enlarged views at the AISI 441 interface).

In brief, the above aging test demonstrates that YSZ/AISI 441 joints obtained with the Ag particle interlayer presented long-term (≥300 h) stability in both a wet reducing atmosphere and oxidizing atmosphere. Due to the absence of CuO, the joints were more stable in a reducing atmosphere on the one hand, and the oxide layer formed on the stainless steel surface was much thinner and denser in the oxidizing atmosphere on the other hand. Compared with the traditional RAB method, the method in this paper can greatly improve the service life of the joint, and is more suitable for fabricating the SOFC/SOEC stacks.

4. Conclusions

In this study, the YSZ electrolyte was successfully joined to the AISI 441 interconnect using the Ag particle interlayer in air under an assembly pressure of ~2 MPa. The microstructure, mechanical properties, and aging properties of the joints were analyzed in-depth. The main conclusions can be summarized as follows:

- (1) Dense and defect-free joints were fabricated at 920 °C/30 min using the Ag particle interlayer. A thin and dense oxide layer (~2 µm) was observed at the Ag/AISI 441 interface. TEM results prove that the interatomic bonding of YSZ/Ag was achieved by forming a diffusion layer with a disordered lattice (~3 nm) between them. Furthermore, the sintering effect played a key role in the joining process.
- (2) No significant defects were observed at the YSZ/Ag interface at the temperature range of 860–950 °C, which can be attributed to the excellent plasticity and sintering properties of Ag particles. The oxide layer at the AISI 441/Ag interface thickened with the increasing temperature. The oxide layer thickness only reached 2–3 µm, even at 950 °C, which was much thinner than the traditional RAB joints (typically ≥20 µm).
- (3) Lower temperatures will lead to insufficient diffusion of YSZ/Ag, resulting in poor bonding strength at the YSZ/Ag interface. In contrast, excessive temperatures can aggravate the oxidation at the AISI 441 interface, thus reducing the AISI 441/Ag interfacial strength. Therefore, the maximum shear strength of the joint (~86.1 MPa) was achieved at 920 °C in air, which was 161% higher than that of traditional RAB joints (~33 MPa).
- (4) Aging tests demonstrate that YSZ/AISI 441 joints obtained with the Ag particle interlayer presented superior long-term (≥300 h) stability in both reducing and oxidizing atmospheres. The joints were more stable in the reducing atmosphere due to the absence of CuO decomposition. Additionally, the oxide layer along the steel interconnect interface was much thinner and denser in the oxidizing atmosphere without the severe reactions between the CuO and steel.

This study shows that the YSZ/AISI 441 joints fabricated by the Ag particle interlayer possess enhanced mechanical and aging properties, which may improve the reliability and service life of SOFC/SOEC stacks. Meanwhile, the low-cost and high-quality Ag particle interlayer sintering joining method proposed in this paper provides a new idea for metal/ceramic joining. Furthermore, this method can be combined with field-assisted sintering technology (such as electric field-assisted), which may further reduce the joining temperature and improve the interfacial strength. Furthermore, this method seems to be equally applicable for joining SOFC/SOEC electrode materials and interconnects. In the future, the joining of various electrode materials to the interconnect via the particle Ag interlayer can be further studied, and the aging performance of corresponding joints in the actual operating environment can be tested.

Supplementary Materials: The following are available online at <https://www.mdpi.com/article/10.3390/cryst11121573/s1>, Figure S1: Schematic diagram of preparation of wet reducing atmosphere, Figure S2: (a) Overview SEM image and (b) interfacial microstructure of YSZ/AISI 441 joints obtained at 970 °C for 30 min, Figure S3: Fracture surfaces at (a) 890 °C and (b) 950 °C at the YSZ side, Figure S4: The shear stress–shear displacement curve of joints obtained at various temperatures.

Author Contributions: X.S.: Methodology, Supervision, Validation, Conceptualization, Data curation, Writing-review & editing. X.W.: Investigation, Formal analysis, Validation, Visualization, Methodology, Data curation, Writing-original draft, Writing-review & editing. C.L.: Methodology, Data curation, Writing-review & editing. T.L.: Writing-review & editing. J.Q.: Writing-review & editing. J.C.: Funding acquisition, Resources, Project administration, Supervision, Writing-review & editing. All authors have read and agreed to the published version of the manuscript.

Funding: This research was funded by the National Natural Science Foundation of China under Grant U1737205 and 52005131; the Postdoctoral Science Foundation of China 2019TQ0075; and the Heilongjiang Provincial Postdoctoral Science Foundation LBH-Z19142.

Institutional Review Board Statement: Not applicable.

Informed Consent Statement: Not applicable.

Data Availability Statement: The raw/processed data required to reproduce these findings cannot be shared at this time as the data also forms part of an ongoing study.

Acknowledgments: Thank Qing Du, Yongchun Zou, Daqing Wei, Baoyou Zhang and Shu Guo from the analysis and testing center of Harbin Institute of technology for their help in analysis and testing.

Conflicts of Interest: The authors declare no conflict of interest.

References

1. Xu, N.; Zhu, T.; Yang, Z.; Han, M. Fabrication and optimization of $\text{La}_{0.4}\text{Sr}_{0.6}\text{Co}_{0.2}\text{Fe}_{0.7}\text{Nb}_{0.1}\text{O}_{3-\delta}$ electrode for symmetric solid oxide fuel cell with zirconia based electrolyte. *J. Mater. Sci. Technol.* **2017**, *33*, 1329–1333. [\[CrossRef\]](#)
2. Sezer, H.; Mason, J.H.; Celik, I.B.; Yang, T. Three-dimensional modeling of performance degradation of planar SOFC with phosphine exposure. *Int. J. Hydrog. Energy* **2021**, *46*, 6803–6816. [\[CrossRef\]](#)
3. Si, X.; Cao, J.; Ritucci, I.; Talic, B.; Feng, J.; Kiebach, R. Enhancing the long-term stability of Ag based seals for solid oxide fuel/electrolysis applications by simple interconnect aluminization. *Int. J. Hydrog. Energy* **2019**, *44*, 3063–3074. [\[CrossRef\]](#)
4. Kong, W.; Zhang, W.; Huang, H.; Zhang, Y.; Wu, J.; Xu, Y. Analysis of micro-tubular SOFC stability under ambient and operating temperatures. *J. Mater. Sci. Technol.* **2018**, *34*, 1436–1440. [\[CrossRef\]](#)
5. Lyu, Y.; Xie, J.; Wang, D.; Wang, J. Review of cell performance in solid oxide fuel cells. *J. Mater. Sci.* **2020**, *55*, 7184–7207. [\[CrossRef\]](#)
6. Tucker, M.C. Progress in metal-supported solid oxide fuel cells: A review. *J. Power Sources* **2010**, *195*, 4570–4582. [\[CrossRef\]](#)
7. Wang, Z.; Li, C.; Si, X.; Yang, B.; Huang, Y.; Qi, J.; Feng, J.; Cao, J. Brazing YSZ ceramics by a novel SiO_2 nanoparticles modified Ag filler. *Ceram. Int.* **2020**, *46*, 16493–16501. [\[CrossRef\]](#)
8. Han, M.; Tang, X.; Yin, H.; Peng, S. Fabrication, microstructure and properties of a YSZ electrolyte for SOFCs. *J. Power Sources* **2007**, *165*, 757–763. [\[CrossRef\]](#)
9. Wang, Y.; Li, W.; Ma, L.; Li, W.; Liu, X. Degradation of solid oxide electrolysis cells: Phenomena, mechanisms, and emerging mitigation strategies—A review. *J. Mater. Sci. Technol.* **2020**, *55*, 35–55. [\[CrossRef\]](#)
10. Chen, S.; Gu, D.; Zheng, Y.; Chen, H.; Guo, L. Enhanced performance of NiO–3YSZ planar anode-supported SOFC with an anode functional layer. *J. Mater. Sci.* **2020**, *55*, 88–98. [\[CrossRef\]](#)
11. Blum, L.; Meulenber, W.A.; Nabielek, H.R. Steinberger-Wilckens, Worldwide SOFC Technology Overview and Benchmark. *Int. J. Appl. Ceram. Technol.* **2005**, *2*, 482–492. [\[CrossRef\]](#)
12. Jeon, S.K.; Nahm, S.H.; Kwon, O.H. Improvement in the Adhesion between Electrode of a SOFC and Ag Paste as a Current Collector by Au Deposition. *J. Mater. Sci. Technol.* **2015**, *31*, 257–263. [\[CrossRef\]](#)
13. Ferraris, M.; De la Pierre, S.; Sabato, A.G.; Smeacetto, F.; Javed, H.; Walter, C.; Malzbender, J. Torsional shear strength behavior of advanced glass-ceramic sealants for SOFC/SOEC applications. *J. Eur. Ceram. Soc.* **2020**, *40*, 4067–4075. [\[CrossRef\]](#)
14. Wu, J.; Liu, X. Recent Development of SOFC Metallic Interconnect. *J. Mater. Sci. Technol.* **2010**, *26*, 293–305. [\[CrossRef\]](#)
15. Mahmud, L.S.; Muchtar, A.; Somalu, M.R. Challenges in fabricating planar solid oxide fuel cells: A review. *Renew. Sustain. Energy Rev.* **2017**, *72*, 105–116. [\[CrossRef\]](#)
16. Sabzi, M.; Mousavi Anijdan, S.H.; Eivani, A.R.; Park, N.; Jafarian, H.R. The effect of pulse current changes in PCGTAW on microstructural evolution, drastic improvement in mechanical properties, and fracture mode of dissimilar welded joint of AISI 316L-AISI 310S stainless steels. *Mater. Sci. Eng. A* **2021**, *823*, 141700. [\[CrossRef\]](#)
17. Sabzi, M.; Dezfuli, S.M. Drastic improvement in mechanical properties and weldability of 316L stainless steel weld joints by using electromagnetic vibration during GTAW process. *J. Manuf. Process.* **2018**, *33*, 74–85. [\[CrossRef\]](#)
18. Mousavi Anijdan, S.H.; Sabzi, M.; Ghobeiti-Hasab, M.; Roshan-Ghiyas, A. Optimization of spot welding process parameters in dissimilar joint of dual phase steel DP600 and AISI 304 stainless steel to achieve the highest level of shear-tensile strength. *Mater. Sci. Eng. A* **2018**, *726*, 120–125. [\[CrossRef\]](#)
19. Reza Tabrizi, T.; Sabzi, M.; Mousavi Anijdan, S.H.; Eivani, A.R.; Park, N.; Jafarian, H.R. Comparing the effect of continuous and pulsed current in the GTAW process of AISI 316L stainless steel welded joint: Microstructural evolution, phase equilibrium, mechanical properties and fracture mode. *J. Mater. Res. Technol.* **2021**, *15*, 199–212. [\[CrossRef\]](#)
20. Kiebach, R.; Engelbrecht, K.; Grahl-Madsen, L.; Sieborg, B.; Chen, M.; Hjelm, J.; Norrman, K.; Chatzichristodoulou, C.; Hendriksen, P.V. An Ag based brazing system with a tunable thermal expansion for the use as sealant for solid oxide cells. *J. Power Sources* **2016**, *315*, 339–350. [\[CrossRef\]](#)
21. Zhu, W.Z.; Deevi, S.C. Development of interconnect materials for solid oxide fuel cells. *Mater. Sci. Eng. A* **2003**, *348*, 227–243. [\[CrossRef\]](#)
22. Si, X.; Cao, J.; Talic, B.; Ritucci, I.; Li, C.; Qi, J.; Feng, J.; Kiebach, R. A novel Ag based sealant for solid oxide cells with a fully tunable thermal expansion. *J. Alloys Compd.* **2020**, *831*, 154608. [\[CrossRef\]](#)
23. Si, X.; Cao, J.; Song, X.; Qu, Y.; Feng, J. Reactive air brazing of YSZ ceramic with novel Al_2O_3 nanoparticles reinforced Ag-CuO- Al_2O_3 composite filler: Microstructure and joint properties. *Mater. Des.* **2017**, *114*, 176–184. [\[CrossRef\]](#)
24. Si, X.; Cao, J.; Song, X.; Wang, Z.; Wang, Z.; Feng, J. Evolution behavior of Al_2O_3 nanoparticles reinforcements during reactive air brazing and its role in improving the joint strength. *Mater. Des.* **2017**, *132*, 96–104. [\[CrossRef\]](#)
25. Zhao, Y.; Beck, T. *Thermo-Mechanical Properties of Glass-Ceramic Solid Oxide Fuel Cell Sealant Materials*; Lehrstuhl für Werkstoffe der Energietechnik (FZ Jülich): Aachen, Germany, 2013; p. 141.
26. Smeacetto, F.; Chrysanthou, A.; Salvo, M.; Zhang, Z.; Ferraris, M. Performance and testing of glass-ceramic sealant used to join anode-supported-electrolyte to Crofer22APU in planar solid oxide fuel cells. *J. Power Sources* **2009**, *190*, 402–407. [\[CrossRef\]](#)

27. Shyam, A.; Trejo, R.; McClurg, D.; Ladouceur, A.; Kirkham, M.; Song, X.; Howe, J.; Lara-Curzio, E. Microstructural evolution in two alkali multicomponent silicate glasses as a result of long-term exposure to solid oxide fuel cell environments. *J. Mater. Sci.* **2013**, *48*, 5880–5898. [[CrossRef](#)]
28. Chang, H.-T.; Lin, C.-K.; Liu, C.-K. Effects of crystallization on the high-temperature mechanical properties of a glass sealant for solid oxide fuel cell. *J. Power Sources* **2010**, *195*, 3159–3165. [[CrossRef](#)]
29. Reis, S.T.; Pascual, M.J.; Brow, R.K.; Ray, C.S.; Zhang, T. Crystallization and processing of SOFC sealing glasses. *J. Non-Cryst. Solids* **2010**, *356*, 3009–3012. [[CrossRef](#)]
30. Bobzin, K.; Öte, M.; Wiesner, S.; Kaletsch, A.; Broeckmann, C. Characterization of Reactive Air Brazed Ceramic/Metal Joints with Unadapted Thermal Expansion Behavior: RAB Joints with Unadapted Thermal Expansion Behavior. *Adv. Eng. Mater.* **2014**, *16*, 1490–1497. [[CrossRef](#)]
31. Cao, J.; Wang, Z.; Li, C.; Si, X.; Yang, B.; Guo, X.; Huang, Y.; Qi, J. Microstructure evolution and mechanical properties of Co coated AISI 441 ferritic stainless steel/ YSZ reactive air brazed joint. *Int. J. Hydrog. Energy* **2021**, *46*, 8758–8766. [[CrossRef](#)]
32. Raju, K.; Muksin; Kim, S.; Song, K.; Yu, J.H.; Yoon, D.-H. Joining of metal-ceramic using reactive air brazing for oxygen transport membrane applications. *Mater. Des.* **2016**, *109*, 233–241. [[CrossRef](#)]
33. Weil, K.S.; Kim, J.Y.; Hardy, J.S. Reactive Air Brazing: A Novel Method of Sealing SOFCs and Other Solid-State Electrochemical Devices. *Electrochem. Solid-State Lett.* **2005**, *8*, A133. [[CrossRef](#)]
34. Kaletsch, A. Effects of Copper Oxide Content in AgCuO Braze Alloy on Microstructure and Mechanical Properties of Reactive-Air-Brazed Ba_{0.5}Sr_{0.5}Co_{0.8}Fe_{0.2}O_{3-δ} (BSCF). *J. Ceram. Sci. Technol.* **2012**, *3*, 95–103. [[CrossRef](#)]
35. Chatzimichail, R.; Triantafyllou, G.; Tietz, F.; Nikolopoulos, P. Interfacial properties of (Ag + CuO) brazes used as sealing materials in SOFC stacks. *J. Mater. Sci.* **2014**, *49*, 300–313. [[CrossRef](#)]
36. Kim, J.; Hardy, J.; Weil, S. Dual-atmosphere tolerance of Ag–CuO-based air braze. *Int. J. Hydrog. Energy* **2007**, *32*, 3655–3663. [[CrossRef](#)]
37. Kuhn, B.; Wetzell, F.J.; Malzbender, J.; Steinbrech, R.W.; Singheiser, L. Mechanical performance of reactive-air-brazed (RAB) ceramic/metal joints for solid oxide fuel cells at ambient temperature. *J. Power Sources* **2009**, *193*, 199–202. [[CrossRef](#)]
38. Kuhn, B.; Wessel, E.; Malzbender, J.; Steinbrech, R.W.; Singheiser, L. Effect of isothermal aging on the mechanical performance of brazed ceramic/metal joints for planar SOFC-stacks. *Int. J. Hydrog. Energy* **2010**, *35*, 9158–9165. [[CrossRef](#)]
39. Zhou, Q.; Bieler, T.R.; Nicholas, J.D. Transient porous nickel interlayers for improved silver-based Solid Oxide Fuel Cell brazes. *Acta Mater.* **2018**, *148*, 156–162. [[CrossRef](#)]
40. Phongpreecha, T.; Nicholas, J.D.; Bieler, T.R.; Qi, Y. Computational design of metal oxides to enhance the wetting and adhesion of silver-based brazes on yttria-stabilized-zirconia. *Acta Mater.* **2018**, *152*, 229–238. [[CrossRef](#)]
41. Pönicke, A.; Schilm, J.; Kusnezoff, M.; Michaelis, A. Aging Behavior of Reactive Air Brazed Seals for SOFC. *Fuel Cells* **2015**, *15*, 735–741. [[CrossRef](#)]
42. Scott Weil, K.; Coyle, C.A.; Darsell, J.T.; Xia, G.G.; Hardy, J.S. Effects of thermal cycling and thermal aging on the hermeticity and strength of silver-copper oxide air-brazed seals. *J. Power Sources* **2005**, *152*, 97–104. [[CrossRef](#)]
43. Zeng, Z.; Qian, Y.; Zhang, Y.; Hao, C.; Dan, D.; Zhuge, W. A review of heat transfer and thermal management methods for temperature gradient reduction in solid oxide fuel cell (SOFC) stacks. *Appl. Energy* **2020**, *280*, 115899. [[CrossRef](#)]
44. Ding, J.; Zhou, X.; Liu, Q.; Yin, G. Development of tubular anode-supported solid oxide fuel cell-cell and 4-cell-stack based on lanthanum gallate electrolyte membrane for mobile application. *J. Power Sources* **2018**, *401*, 336–342. [[CrossRef](#)]
45. Yeom, J.; Nagao, S.; Chen, C.; Sugahara, T.; Zhang, H.; Choe, C.; Li, C.-F.; Sugauma, K. Ag particles for sinter bonding: Flakes or spheres? *Appl. Phys. Lett.* **2019**, *114*, 253103. [[CrossRef](#)]
46. Kim, M.I.; Choi, E.B.; Lee, J.-H. Improved sinter-bonding properties of silver-coated copper flake paste in air by the addition of sub-micrometer silver-coated copper particles. *J. Mater. Res. Technol.* **2020**, *9*, 16006–16017. [[CrossRef](#)]
47. Wang, Z.; Li, C.; Si, X.; Liu, Y.; Qi, J.; Huang, Y.; Feng, J.; Cao, J. Oxidation behavior of ferritic stainless steel interconnect coated by a simple diffusion bonded cobalt protective layer for solid oxide fuel cells. *Corros. Sci.* **2020**, *172*, 108739. [[CrossRef](#)]
48. Alnegren, P.; Sattari, M.; Svensson, J.-E.; Froitzheim, J. Temperature dependence of corrosion of ferritic stainless steel in dual atmosphere at 600–800 °C. *J. Power Sources* **2018**, *392*, 129–138. [[CrossRef](#)]
49. Gunduz, K.O.; Chyrkin, A.; Goebel, C.; Hansen, L.; Hjorth, O.; Svensson, J.-E.; Froitzheim, J. The effect of hydrogen on the breakdown of the protective oxide scale in solid oxide fuel cell interconnects. *Corros. Sci.* **2021**, *179*, 109112. [[CrossRef](#)]
50. Xu, Y.; Wen, Z.; Wang, S.; Wen, T. Cu doped Mn–Co spinel protective coating on ferritic stainless steels for SOFC interconnect applications. *Solid State Ion.* **2011**, *192*, 561–564. [[CrossRef](#)]
51. Molin, S.; Jasinski, P.; Mikkelsen, L.; Zhang, W.; Chen, M.; Hendriksen, P.V. Low temperature processed MnCo₂O₄ and MnCo_{1.8}Fe_{0.2}O₄ as effective protective coatings for solid oxide fuel cell interconnects at 750 °C. *J. Power Sources* **2016**, *336*, 408–418. [[CrossRef](#)]
52. Si, X.; Cao, J.; Kiebach, R.; Xu, Y.; Xu, H.; Talic, B.; Feng, J. Joining of solid oxide fuel/electrolysis cells at low temperature: A novel method to obtain high strength seals already at 300 °C. *J. Power Sources* **2018**, *400*, 296–304. [[CrossRef](#)]
53. German, R.M. 1-Thermodynamics of sintering. In *Sintering of Advanced Materials*; Elsevier: Amsterdam, The Netherlands, 2010; pp. 3–32. [[CrossRef](#)]
54. Chen, T.F.; Siow, K.S. Comparing the mechanical and thermal-electrical properties of sintered copper (Cu) and sintered silver (Ag) joints. *J. Alloys Compd.* **2021**, *866*, 158783. [[CrossRef](#)]

-
55. Bai, J.G.; Yin, J.; Zhang, Z.; Lu, G.-Q.; van Wyk, J.D. High-Temperature Operation of SiC Power Devices by Low-Temperature Sintered Silver Die-Attachment. *IEEE Trans. Adv. Packag.* **2007**, *30*, 506–510. [[CrossRef](#)]
 56. Gadaud, P.; Caccuri, V.; Bertheau, D.; Carr, J.; Milhet, X. Ageing sintered silver: Relationship between tensile behavior, mechanical properties and the nanoporous structure evolution. *Mater. Sci. Eng. A* **2016**, *669*, 379–386. [[CrossRef](#)]
 57. Chen, C.; Suganuma, K. Microstructure and mechanical properties of sintered Ag particles with flake and spherical shape from nano to micro size. *Mater. Des.* **2019**, *162*, 311–321. [[CrossRef](#)]
 58. Hu, G.; Zhou, Q.; Bhatlawande, A.; Park, J.; Termuhlen, R.; Ma, Y.; Bieler, T.R.; Yu, H.-C.; Qi, Y.; Hogan, T.; et al. Patterned nickel interlayers for enhanced silver wetting, spreading and adhesion on ceramic substrates. *Scr. Mater.* **2021**, *196*, 113767. [[CrossRef](#)]
 59. Sabzi, M.; Obeydavi, A.; Mousavi Anijdan, S.H. The effect of joint shape geometry on the microstructural evolution, fracture toughness, and corrosion behavior of the welded joints of a Hadfield Steel. *Mech. Adv. Mater. Struct.* **2019**, *26*, 1053–1063. [[CrossRef](#)]